Design and Performance Analysis of an Automated 10-Channel Solar Radiometer Instrument

A. R. EHSANI, J. A. REAGAN, AND W. H. ERXLEBEN

Electrical and Computer Engineering Department, The University of Arizona, Tucson, Arizona

ABSTRACT

An automated multichannel solar radiometer has been designed and fabricated by the Atmospheric Remote Sensing Laboratory at The University of Arizona. The automated radiometer has 10 separate silicon-photodiode-based channels that allow near-simultaneous solar spectral measurements through narrow bandpass filters (approximately 10 nm) from the visible to near-IR regions. The photodiode detectors are temperature stabilized using a heating temperature controller circuit. The instrument is pointed toward the sun via an autotracking system that actively tracks the sun with a ±0.05° tracking accuracy. The instrument can continuously collect data for about 22 h at once per minute sample rate. This paper presents instrument design features as well as some performance and experimental results for the automated solar radiometer.

1. Introduction

Over the past decade, the Atmospheric Remote Sensing Laboratory (ARSL) at The University of Arizona has built a number of portable and manually operated solar radiometers that have been used in a variety of atmospheric correction and spectral transmittance measurement applications (e.g., Bruegge et al. 1992; Moore et al. 1989; Reagan et al. 1987a; Slater et al. 1987; Teillet et al. 1990). These radiometers consist of a filter wheel placed between a silicon detector and telescope. They operate by manually pointing the telescope toward the sun and rotating the filter wheel to select the desired wavelength (10 wavelengths). The signal generated by the detector is amplified, digitized, and displayed for manual recording. Although data collected with the manual solar radiometers have proven to be reliable and advantageous, the process of data collection is tedious and time consuming, typically requiring at least 1 min to run through all 10 wavelengths. As such, the manual instrument is not effective under rapidly temporally varying atmospheric conditions as well as requiring constant attention for operation. The need for a new generation of automated solar radiometers was apparent.

An automated solar radiometer was designed and fabricated to address the above shortcomings. The new multichannel solar radiometer system shown in Fig. 1 is used in monitoring atmospheric spectral transmittance over a wavelength range from 380 to 1030 nm. The solar radiometer consists of 10 parallel telescopes, which are all pointed toward the sun via a quadrant

Corresponding author address: Prof. John A. Reagan, Dept. of ECE, The University of Arizona, P.O. Box 210104, Tucson, AZ 85721-0104.

detector-based automated sun-tracking system with a ±0.05° maximum tracking error. Each channel consists of a telescope with a field of view (FOV) defined by a set of clear apertures [3.2° full width half maximum (FWHM) FOV], an interference filter (approximately 10-nm bandpass), and a silicon photodiode/op amp combination. The temperature of each photodiode/op amp module is stabilized with a temperature controller to ensure uniform responsivity of the detectors throughout the course of data collection. The gain of each operational amplifier is selected to match the dynamic range of the radiometer data acquisition system (DAS). The DAS controls all the activities of the solar radiometer system and is initialized by a menu-driven program. The automated DAS controls sun tracking, monitors the temperature of the detectors as well as the output of all 10 channels, and writes these values to the internal memory, along with the time of data collection. At the end of a data collection period, the DAS can be hooked up to a personal computer to transfer the collected data into the computer via the serial port.

2. Instrument features

The automated solar radiometer instrument as shown in Fig. 1 consists of four major parts: (a) radiometer head, (b) tracking mount, (c) DAS, and (d) power supply. The unit as shown is about 60 cm high, and the radiometer head round tube containing the 10 telescopes is 12.7 cm in diameter. The DAS controls all the activities of the automated solar radiometer. The control signals from the DAS are transmitted to the radiometer head and from the radiometer head to the tracking mount stepper motors. A 12-V power supply (for which a 12-
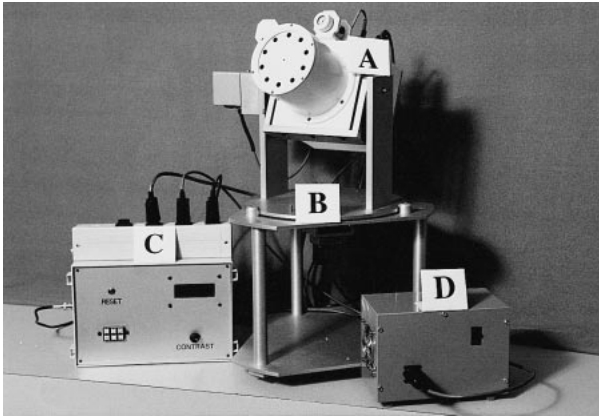
FIG. 1. A picture of the automated 10-channel solar radiometer instrument: (a) radiometer head, (b) tracking mount, (c) data acquisition system (DAS), and (d) power supply.

V car battery may be substituted) is connected directly to the DAS, which includes internal voltage convertors and regulators. The regulated voltages are supplied to the radiometer head and tracking mount from the DAS. The four major components of the automated solar radiometer are described in detail in the following sections.

a. Data acquisition system

A block diagram of the DAS is shown in Fig. 2. The DAS controls all the activities of the instrument through a microcontroller chip (Intel's 87C51FA). The 8-bit microcontroller has 8 kbytes of internal programming memory, which is used for controlling numerous functional capabilities of the instrument. The microcontroller chip controls other devices by writing control data to three latches. The destination of control data is selected by a two-to-four decoder. The output lines of the three latches are connected to a number of devices including

an analog-to-digital converter (ADC) chip, a real-time clock (RTC) chip, a liquid crystal display (LCD) panel, a 16-to-1 analog multiplexer chip, and two stepper-motor driver chips. The DAS circuitry is housed in a weather-sealed plastic box. The instrument is initialized through a six-button keypad with menu-driven options displayed on the LCD (20 characters by four lines).

The DAS collects analog signals from the radiometer head and digitizes the signals to 16-bit binary numbers employing the 16-bit ADC, providing a maximum of 65 535 digital counts. The ADC has a voltage resolution of 69 μV (for a voltage reference of 4.5 V). Random noise and voltage offsets are generally less than 100 counts or less than 0.2% of full scale. The ADC receives an analog signal from the 16-to-1 multiplexer residing in the radiometer head. The analog input to the ADC chip can be selected by controlling the output of the multiplexer through one of the control latches. The output of the latch can select between the analog signals from the 10 detectors, as well as the outputs of the quadrant detector and the temperature-reading signal. The microcontroller uses the digitized signals of the quadrant detector to control pointing of the radiometer head toward the sun. Once the radiometer head is aligned on the sun, the signals from the 10 detectors and the temperature reading are sequentially sampled and digitized. The time elapsed while reading and storing data from all 10 channels is on the order of a few milliseconds.

The digitized data are stored in a 32-kbyte nonvolatile random access memory (RAM), which is sufficient to store approximately 1300 complete 10-channel datasets (i.e., about 22 h of data collection at a once per minute sample rate). The nonvolatile RAM's internal battery power can last for up to 10 years. The RTC is used to synchronize the data collection time. Clock inaccuracy is less than 1s per day, requiring resetting not more frequently than once per day and generally only once a
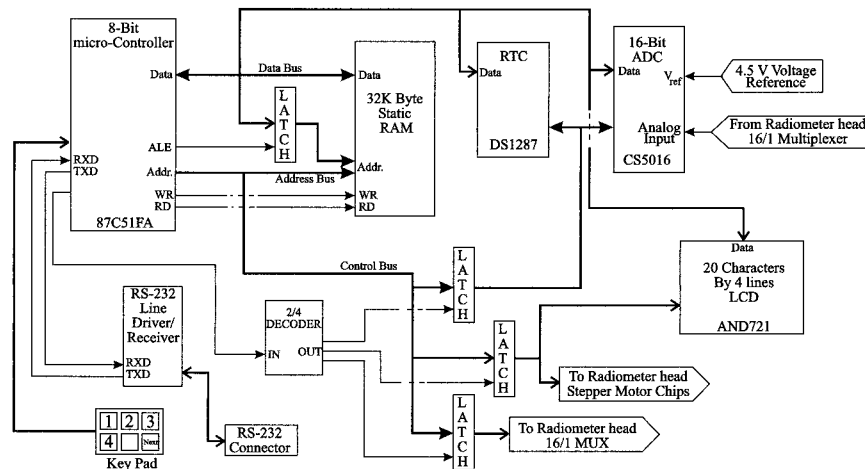
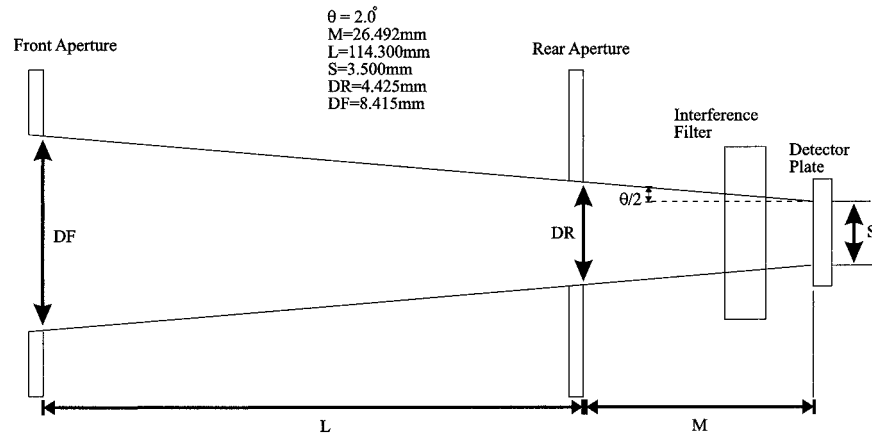

FIG. 2. A block diagram of the DAS.

FIG. 3. The field of view of the 10 identical telescopes is defined by a set of clear apertures and their relative distance to the detector plane.

week. The start time, stop time, and time interval between each data collection can be initialized through the menu-driven options of the DAS. The time interval between each data collection can be selected from as short as every 10 s to as long as every 15 min. If desired, the collection rate option could be extended beyond this range by changing the microcontroller firmware. The DAS provides the option of overwriting previously collected data or to continue storing data to the end of the last data collection set. This option allows the operator to collect data at a number of different times before downloading the collected data into a computer. This feature is useful if one wants to collect short datasets at infrequent times and/or move the radiometer from one collection site to another. A number displayed on the upper right-hand side of the LCD indicates the number of data collection periods remaining within the memory space such that for every data collection sequence this number is reduced by one. However, once the 32-kbyte limit of the internal RAM is reached, the DAS will automatically stop data collection. The data stored in the DAS memory can be transferred to a computer through the RS-232 port at a 9600-baud rate.

b. Power supply requirements

The solar radiometer instrument can be powered by a 12-V dc power supply or a 12-V dc battery. A dc-to-dc convertor inside the DAS generates the −12 V required for biasing the detector amplifiers. The −12 voltage is also converted to the −5 V needed for the ADC chip. The +12 voltage is also converted to +5 V, which is the required voltage for most logic chips/devices. Because most of the electric power is used to stabilize the temperature of the detectors to 43°C, the average power consumption of the instrument depends on the surrounding temperature. The peak power drain for initial heating of the detector heater plate can run as high as approximately 38 W but is typically less than 4 W after the

temperature is stabilized. The data stored in the DAS during or after data collection are protected against power failures. The data are kept in the nonvolatile, backup battery-protected RAM of the DAS and can be transmitted through the serial port to a personal computer at any time.

c. Radiometer head

The radiometer head consists of 10 parallel telescopes, which are all pointed toward the sun via an autotracking system that actively tracks the sun. The solar irradiance transmitted through each telescope is then passed through an interference filter and detected by a detector/op amp combination module. Interference filters are placed between the rear apertures of the telescopes and the detector photodiodes. The 10 interference filters have narrow bandpasses of approximately 10 nm each and are spaced fairly uniformly in the visible and near-IR regions; center wavelengths are selected to avoid strong gaseous spectral absorption lines except for one placed in a water absorption band. The center wavelengths are typically 380, 400, 440, 520, 610, 670, 780, 870, 940, and 1030 nm, with the 940-nm channel being the water vapor absorption channel.

The geometry of the telescope is shown in Fig. 3. The telescope FOV half-angle is calculated from

$$\frac{\theta}{2} = \tan^{-1}\frac{DF - DR}{2L}, \tag{1}$$

where DF is the front aperture diameter, DR is the rear aperture diameter, and L is the distance between the front and rear apertures. This equation defines the half-angle range that allows full illumination of spot size S by off-axis rays entering the telescope. The aperture diameters and separation distance (listed in Fig. 3) were selected to yield a half-angle of $\theta/2 = 1°$. This design purposely overfills the detector, which has a diameter ($D_d = 2.54$ mm) smaller than S, to allow some tolerance for posi-
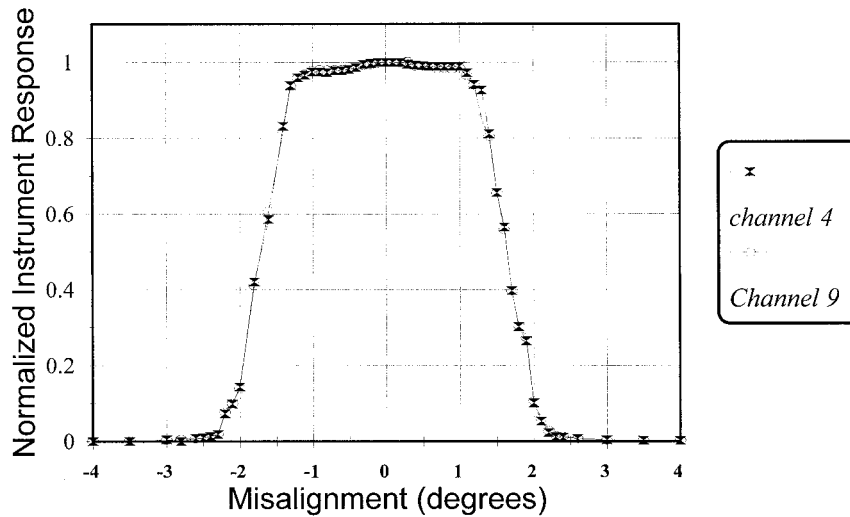
FOV Measurements

Fig. 4. Experimental measurements of the FOV for channels 4 and 9.

tioning the detector plate assembly. If D_d is substituted for DR and $(L + M)$ for L in Eq. (6), a half-angle of $\theta/2 = 1.2°$ is obtained. Given that the sun subtends an angle of approximately 0.56°, the outer edge of the solar disk would start to be obscured by the aperture when the sun's central ray is about 0.92° off in alignment from the telescope's axis. Hence, the detector response should remain nearly constant for tracking errors to approximately ±1°.

The accuracy of the 10 parallel telescopes was experimentally tested to verify the telescope FOV half-angles and their coalignments. The outputs of the solar radiometer channels were measured by first aligning the solar radiometer on sun (via the autotracking system) and then stepping the radiometer in 0.1° steps (in both positive and negative elevation directions) to a specified off-axis angular position (i.e., to 0.1°, 0.2°, 0.3°, . . . through 4.0°). Aligning on the sun before each off-axis measurement provided an on-axis normalization signal taken within a few seconds of each off-axis measurement, thereby removing bias effects due to temporally varying atmospheric transmittance over the several minutes required to complete the ±4.0° scan. The results of the measured normalized outputs for channels 4 and 9 (520 and 940 nm) are plotted in Fig. 4. All the other channels exhibited similar results. From this figure it can be seen that, as expected, the outputs of the two channels start to significantly decline at about ±1° angular misalignment. These scan results also show that the FWHM FOV of the telescope is approximately 3.2°.

The maximum FOV half-angle for which source radiation can still fall on the detector is given by

$$\frac{\theta_m}{2} = \tan^{-1}\left[\frac{DF + D_d}{2(L + M)}\right]. \qquad (2)$$

From Eq. (2) and the parameters listed in Fig. 3, the predicted maximum FOV half-angle $\theta_m/2 = 2.23°$. This predicted angle is also consistent with the experimental results shown in Fig. 4. The truly flat response region in Fig. 4 is for a misalignment range within approximately ±0.25°. This is 10 times the angular step resolution of the stepper motors used to actively align the telescope on the sun.

The silicon photodiode detectors (EG&G HUV-1100BG) have a 5.1-mm² active area and a built-in operational amplifier. The detectors are operated in the photovoltaic mode (i.e., no reverse bias), which produces a current proportional to the light power incident on the active area of each detector (so long as the photojunctions do not become forward biased by the generated photocurrents). Photovoltaic detectors are designed for low noise and low-frequency applications; below 1 kHz, photovoltaic detectors are generally superior to photoconductive mode (reverse biased) photodiodes in SNR (signal-to-noise ratio) performance. The current generated in each detector is converted to a voltage by a transimpedance amplifier configuration. In a transimpedance configuration, the output voltage of the amplifier is equal to the output current of the detector multiplied by the feedback resistor used with the amplifier. The feedback resistors for each of the 10 amplifiers are selected to match the dynamic range of the DAS (maximum of 4.5 V). A 16-to-1 analog multiplexer is used to select any of the 10 analog output channels to be digitized by the 16-bit ADC of the DAS.

Silicon photodiode responsivities vary with temperature near the short and long wavelength limits of the spectral detection range. To ensure uniform responsivity, the detectors are thermally contacted to an aluminum plate, which is warmed by heating elements and kept
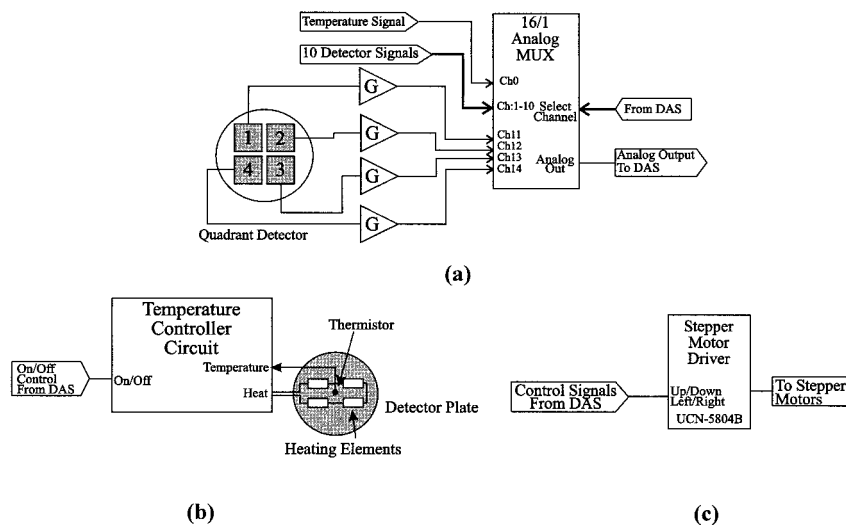
FIG. 5. A block diagram of the circuit components in the radiometer head. (a) The signals connected to the 16/1 analog multiplexer. (b) Temperature controller circuit. (c) Stepper-motor driver chip.

at 43°C via feedback control. The temperature controller circuit shown in block form in Fig. 5 is capable of maintaining the desired temperature within approximately ±0.3°C. A thermistor placed on the detector plate feeds the sensed temperature back to the temperature controller circuit. Once the 43°C set temperature is reached, the temperature controller circuit turns itself on and off periodically to maintain this temperature. The on/off current switching causes a fluctuation in the amount of current drawn from the power supply, possibly introducing noise on the signal lines. To avoid this possibility, measurements of the 10 channels are collected while the temperature controller circuit is turned off. This is done from the DAS through control of a relay switch. The DAS turns off the heating circuit before digitizing the outputs of the 10 channels and turns the heating circuit back on once the measurements are completed. The time process for reading all 10 channels by the DAS is only on the order of milliseconds. The DAS also uses the relay switch to turn off the heating circuit at the end of a data collection period. This is a useful feature when the operator is not available to shut down the system at the stop time of data collection, thus saving power (important if system is battery powered).

The spectral temperature sensitivity of the photodiode was checked by operating two instruments side by side with one instrument already temperature stabilized (at approximately 43°C) and then turning on the temperature controller of the other instrument (which was at a starting temperature of approximately 23°C). This was done around noon when the channel signals of the stabilized instrument changed very little in the short time (approximately 10 min) required to bring the record instrument up to temperature. The channel output voltage displayed no discernable signal change for the approximately 20°C temperature swing, except for the

1030-nm channel, which exhibited a change of approximately 0.5% per degree Celsius.

As shown in Fig. 5, the inputs of the 16-to-1 analog multiplexer are connected to the 10 detector channels, the temperature signal, and the four detectors of the quadrant detector. The current generated in the four detectors of the quadrant detector are amplified to measurable voltage levels by two amplifiers (shown as one amplifier of gain G in Fig. 5) for each detector. The first amplifier acts as a transimpedance amplifier, while the second is an inverting amplifier that produces a positive output voltage. A positive output voltage is required since the ADC of the DAS is hard wired to digitize only positive analog voltages (thus utilizing the full resolution range of the ADC chip).

d. Tracking mount controller

The tracking mount is controlled via two stepper motors (PAS-3206-001 by Hurst Manufacturing Corporation) in the altitude and azimuth directions. The stepper motors have a 0.025° stepping resolution and are controlled by the DAS through the radiometer head's stepper-motor driver chips (see Fig. 5). The two TTL input signals to the stepper-motor driver chips are stepping pulses and direction of motion. The stepping frequency generated by the microcontroller chip of the DAS is approximately 130 Hz. This implies that the tracking mount is capable of movements at a rate of 3.25° per second. The choice of stepping frequency is related to the running torque of the stepper motor. The 130-Hz frequency results in a torque level equal to about 86% of the maximum running torque level of the stepper motor. When the stepper motors are being pulsed, the inductance of the stepper motors induces a considerable amount of noise on the analog ground signal. This noise
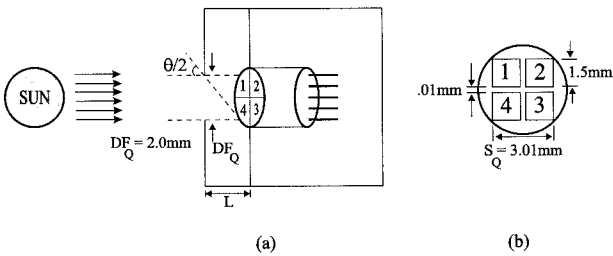
FIG. 6. A quadrant detector is used in the active sun-tracking system. (a) The geometrical aperture-defined FOV telescope for the active tracking mechanism and (b) dimensions of the quadrant detector.

can especially affect the accuracy of the ADC. To eliminate the possibility, the output-enable of the stepper-motor driver chips is employed to disconnect the stepper-motor coils from the rest of the radiometer head circuit before any data are collected.

A quadrant detector (SD-085-23-21-021 by Silicon Detector Corporation) housed in a simple aperture telescope (shown in Fig. 6) is used for sensing the position of the sun. The quadrant detector is made of four square-shaped (1.5 mm each side) silicon detectors, which are separated from one another by 0.01 mm. The quadrant detector is positioned behind the circular entrance aperture of the telescope, as shown in Fig. 6. The circular entrance aperture DF_Q has a diameter of 2.0 mm, which is smaller than the diameter of the quadrant detector, S_Q (4.26 mm). This results in underfilling the quadrant detector by solar illumination. The distance L_Q between the quadrant detector and the circular aperture defines the resolution and FOV of the tracking optical system. A shorter distance results in a larger FOV and lower tracking resolution. Analogous to Eq. (2) given earlier, the maximum tracking FOV half-angle for this arrangement is given by

$$\frac{\theta}{2}_{\max} = \pm \tan^{-1}\frac{DF_Q + S_Q}{2L_Q}. \tag{3}$$

A separation of 8 mm between the quadrant detector and the circular aperture allows a $\pm19°$ tracking range with a $\pm0.05°$ tracking resolution.

The tracking telescope is attached to the top of the radiometer head and is mechanically adjusted to yield solar alignment of the 10 telescopes of the radiometer head. This is done using a simple but precision-machined pinhole and target (approximate 10-cm pinhole to target separation) assembly on the radiometer head telescope tube. The radiometer telescopes are considered centered on the sun when the pinhole "sun dot" is centered in the target alignment circle. The tracking telescope is adjusted to yield balanced quadrant detector signals when the sun dot is visually centered in the alignment circle (visual centering accuracy estimated to be within approximately 20% of the sun dot diameter or approximately 0.1°). The autotracking system is designed to be able to repeatedly return to this reference

alignment within a pointing uncertainty of $\pm0.05°$. The angular scan results shown in Fig. 4 are consistent with these reference alignment and repeat positioning uncertainties.

When the radiometer head is pointed directly toward the sun, the light passing through the tracking telescope entrance aperture is received equally by all four detectors of the quadrant detector. The DAS converts the analog output voltages of two adjacent quadrants into 16-bit binary numbers. The DAS compares only 4–8 MSBs (most significant bits) of the 16-bit values [masking off 8–12 LSBs (least significant bits) based on the amount of incident light on quadrant detector] to avoid "oscillation." The oscillation occurs when the compared signal voltages from two adjacent detector quadrants do not become equal by driving the stepper motors in either direction. The inequality in the detector quadrant signals is caused by the limited stepping resolution of the stepper motors (0.025°). The sun-tracking program determines the number of bits required to be masked off based on the solar intensity (varies with time and calendar date) and the position of the sun with respect to the quadrant detector's telescope axis.

The solar autotracking system is also capable of tracking the sun through thin clouds. The system's tracking capability is reduced by optically thicker clouds. For the case of thicker clouds, the radiometer points itself toward the brightest spot on the clouds, which may not actually be where the sun is. If thick clouds persist, the solar radiometer can, while searching for a bright spot, lose the sun beyond any possible recovery. If the digitized voltages of two adjacent quadrants do not become equal after 20 s of tracking, the system will stop data collection and display an error message. This condition should occur only if the system is pointed toward a thick cloud or when the sun is outside the quadrant detector's FOV. In such cases, the tracking system must be interrupted to stop the radiometer from wrapping itself up with the signal and tracking motor connecting wires. The data collected by the instrument up to the termination point is automatically saved for later transfer to a personal computer.

3. Data collection procedures

The solar radiometer instrument is automated in the sense that it requires no supervision throughout a data collection sequence under normal atmospheric conditions. Once the operator initializes the instrument with start/stop time and interval time between each data collection, the instrument tracks the sun, collects/stores data from all 10 channels, stores detector plate temperature, and logs the time of data collection. The instrument is initialized through a six-button keypad with menu-driven options displayed on an LCD (20 characters by four lines). The internal memory of the DAS (32K RAM) can store data for a total number of points equivalent to about 22 h of data collection at 1-min time

intervals (i.e., approximately 1300 data collection sets). When the DAS reaches its maximum 32K memory space, the instrument will automatically stop collecting data.

Once the radiometer has been initialized, the automated instrument will wait for the start time. The display at all times shows the current time and the number of free data collection sets left within the 32K RAM. The instrument will track the sun, collect data, and display the pertinent information until the stop time is reached. At that time, the instrument turns off the heating circuit and stops all activities while displaying a message indicating completion of a data collection session. The instrument may then either be turned off with the data held in memory for later read out or connected immediately to a personal computer for downloading the stored data. The data collection mode may be interrupted at any time without loss of any previously collected data. This feature allows the operator to stop the data collection routine before the stop time is reached.

The collected data can be retrieved through serial communications between the DAS and a personal computer via the RS-232 port. A program for data retrieval must be run from the personal computer. The computer program sends a command to the DAS requesting the number of valid data points stored in the RAM. The program will then receive data from the DAS accordingly. Once the data retrieval process is completed, a completion message appears on the DAS's display panel.

4. Optical depth measurement relations

The directly transmitted solar spectral irradiance, F_λ (W m^{-2} nm^{-1}), incident on the instrument may be described by the Beer–Bouguer–Lambert law (e.g., Reagan et al. 1986)

$$F_\lambda = \left(\frac{R_m}{R}\right)^2 F_{0\lambda} e^{-m(\theta)\tau_\lambda}, \qquad (4)$$

where $F_{0\lambda}$ is the zero-airmass solar spectral irradiance at wavelength λ for the mean earth–sun separation distance R_m, R is the distance at the time (day) of observation of F_λ, $m(\theta)$ is the atmospheric relative air mass (i.e., ratio of slant path to vertical distance through atmosphere) at solar zenith angle θ, and τ_λ is the total atmospheric optical depth at λ. Observations on different days are typically normalized to $R = R_m$ for uniform comparison. All subsequent expressions and data presented in this paper are for $R = R_m$. The value of air mass m at the time of observation of F_λ may be accurately determined using solar ephemeris data and airmass models, which account for spherical geometry and atmospheric refraction effects (e.g., Reagan et al. 1986).

The directly transmitted solar spectral irradiance received at the earth's surface is collected over some small but nonzero bandwidth $\Delta\lambda$ (interference filter's band-

width) and over some relatively small receiver area, A_d (active area of the detector). The quasi-monochromatic flux received by each detector is transformed to a current that in turn is converted to a voltage, V_λ, by a transimpedance amplifier configuration. The output voltage V_λ of the instrument may then be expressed in the form

$$V_\lambda = A_d \int_{\Delta\lambda} K_\lambda F_\lambda \, d\lambda, \qquad (5)$$

where K_λ (V W^{-1}) is the system spectral responsivity including the spectral dependence of the photodetector and the interference filter and the gain of the transimpedance amplifier for a given channel (i.e., center wavelength). Here, it is assumed that F_λ is constant over the small detector collection area and that the diffuse light within the 3.2° receiver FOV is negligible.

For a fairly small $\Delta\lambda$ and λ outside any gaseous spectral absorption region, the $\exp[-m(\theta)\tau_\lambda]$ term can be taken outside the integral of (5) so that

$$V_\lambda = V_{0\lambda} e^{-m(\theta)\tau_\lambda} \qquad (6)$$

and

$$V_{0\lambda} = A_d \int_{\Delta\lambda} k_\lambda F_{0\lambda} \, d\lambda \simeq A_d K_\lambda F_{0\lambda} \Delta\lambda, \qquad (7)$$

where $V_{0\lambda}$ is the solar radiometer quasi-spectral output signal for zero air mass (i.e., top of the atmosphere signal).

Assuming optical depth τ_λ is constant over the range of air masses for which measurements V_λ are acquired, a plot of $\ln V_\lambda$ versus $m(\theta)$, a Langley plot, will yield a set of data points distributed along a straight line with slope $-\tau_\lambda$ and intercept $\ln V_{0\lambda}$:

$$\ln V_\lambda = \ln V_{0\lambda} - m(\theta)\tau_\lambda. \qquad (8)$$

This is the so-called long method for retrieving optical depth. Given $V_{0\lambda}$ determined from Langley plots when τ_λ was reasonably constant, optical depths may be retrieved versus time (air mass) for other temporally variable days by the calibrated intercept, *short*, or *instantaneous* retrieval method:

$$\tau_\lambda = \frac{1}{m} \ln\left(\frac{V_{0\lambda}}{V_\lambda}\right). \qquad (9)$$

Error in the zero-airmass calibration voltage, $\Delta V_{0\lambda}$, and offset/quantization bias in the measurements, ΔV_λ, cause uncertainty in the retrieval given by

$$\Delta\tau_\lambda = \frac{1}{m}\left(\frac{\Delta V_{0\lambda}}{V_\lambda} - \frac{\Delta V_\lambda}{V_\lambda}\right). \qquad (10)$$

5. Experimental results

As outlined in the previous section, retrieval of optical depths from solar radiometer observations depends directly or indirectly on Langley plots (i.e., either from

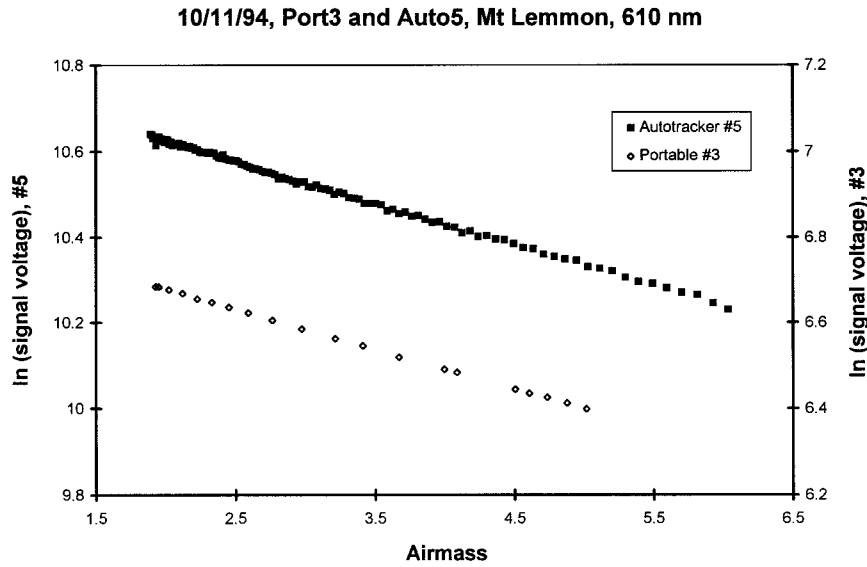**10/11/94, Port3 and Auto5, Mt Lemmon, 610 nm**

FIG. 7. Example Langley plots.

Langley plot slopes on stable days or via zero-airmass intercepts determined from Langley plots on previous stable days). An example stable day Langley plot (for $\lambda \approx 610$ nm) obtained from observations made with one of the automated solar radiometer instruments (#5) at Mt. Lemmon, Arizona (2.8-km elevation), on 11 October 1994 is shown in Fig. 7. Also included is the Langley plot obtained from observations made concurrently with one of our old manually operated filter wheel solar radiometers (#3). The advantages of the autotracker over the manually operated instrument, besides the obvious benefit of automated data collection, are several fold: 1) more accurate solar pointing, 2) higher data sampling rate, 3) more accurate measurement time marking, and 4) higher-resolution digitization. Nevertheless, the manual instrument has proven quite accurate over the years. The optical depths obtained from these two Langley plots ($\tau_{610} \approx 0.10$) agree within 0.002, and other such comparisons (i.e., for fairly small τ_λ; $\tau_{610} <$

$\sim$0.2) have generally yielded agreement within 0.005 for most wavelengths.

Comparing the Langley plot-derived optical depths obtained with two identical type instruments collecting data at the same rate with identical Langley plot data processing provides an overall test of instrument performance. Even if subtle temporal turbidity variations bias the Langley plot slopes, the effects should be the same on both sets of observations, so that any differences in the retrieved optical depths should be attributable to instrument limitations. Comparison results for common wavelengths obtained from observations made with two autotrackers (instruments 14 and 16) on three separate days are given in Table 1 (14 had filters at 410, 501, and 721 nm in place of the normal 400-, 440-, and 520-nm filters). The optical depths were fairly small for all of these days (i.e., $\tau_{611} < 0.119$ and $\tau_{1033} < 0.030$).

What Table 1 actually lists is the difference in optical

TABLE 1. Differences in non-Rayleigh optical depths obtained by two instruments.

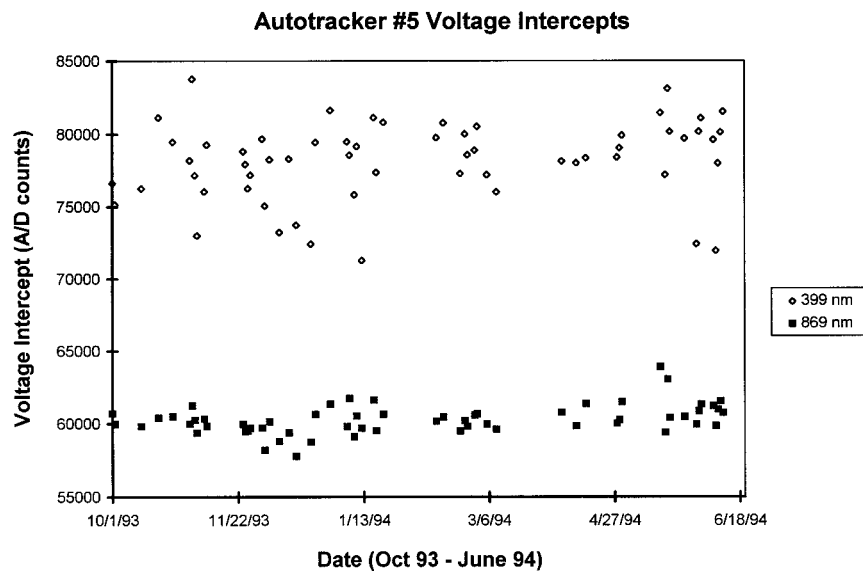|	$(\tau_\lambda - \tau_{\lambda R})_{14} - (\tau_\lambda - \tau_{\lambda R})_{16}$		
Wavelengths	20 Nov 95 Mt. Lemmon	22 Nov 95 Mt. Lemmon	30 Nov 95 Tucson
$\lambda \approx 381$ nm	-0.0037	-0.0028	-0.0065
	$2\sigma_\tau = 0.0007$	$2\sigma_\tau = 0.0005$	$2\sigma_\tau = 0.0022$
$\lambda \approx 611.5$ nm	-0.0008	-0.0007	-0.0017
	$2\sigma_\tau = 0.0008$	$2\sigma_\tau = 0.0005$	$2\sigma_\tau = 0.0015$
$\lambda \approx 669$ nm	0.0007	0.0006	0.0000
	$2\sigma_\tau = 0.0006$	$2\sigma_\tau = 0.0004$	$2\sigma_\tau = 0.0012$
$\lambda \approx 780$ nm	0.0005	0.0013	0.0005
	$2\sigma_\tau = 0.0004$	$2\sigma_\tau = 0.0004$	$2\sigma_\tau = 0.0010$
$\lambda \approx 871.5$ nm	0.001	0.0005	-0.0001
	$2\sigma_\tau = 0.0003$	$2\sigma_\tau = 0.0003$	$2\sigma_\tau = 0.0010$
$\lambda \approx 1033.1$ nm	-0.0007	-0.0011	-0.003
	$2\sigma_\tau = 0.0003$	$2\sigma_\tau = 0.0004$	$2\sigma_\tau = 0.0010$

Autotracker #5 Voltage Intercepts

FIG. 8. Eight-month record of intercept voltages determined from Langley plots.

depths after first subtracting the Rayleigh optical depths, $\tau_{\lambda R}$, for each instrument to compensate for slight differences (approximately 2 nm or less) in the center wavelengths of the filters in each instrument. Given that the channel center wavelength determinations are based on 0.5-nm resolution filter scans, plus any aging effects that may have caused filter wavelength shifts since the filters were last scanned, the values used for $\tau_{\lambda R}$ are still likely to be somewhat in error due to these limitations. For example, an uncertainty in center wavelength of $\Delta\lambda = 0.5$ nm yields an error in $\Delta\tau_{\lambda R} \approx 0.0017$ for a nominal Mt. Lemmon Rayleigh optical depth of $\tau_{\lambda R} = 0.32$ at $\lambda = 380$ nm. Hence, the 380-nm optical depth differences between the two instruments could easily be biased by approximately 0.0035. This bias possibility becomes insignificant at the larger wavelengths because of the sharp λ^{-4} spectral drop-off in $\tau_{\lambda R}$.

Also listed in the table, indicated as $2\sigma_\tau$, is the sum of the optical depth standard deviations for the straight-line Langley plot fits (Langley plot analysis done using technique of Herman et al. 1981) of the data collected by each instrument for a given channel. The optical depth differences should not significantly exceed $2\sigma_\tau$, which is generally true except for the 381-nm channel, again suggesting the likelihood of a wavelength error bias for that channel. The remaining channels yield differences between the two instruments of 0.002 or less, except for one value of 0.003, with most being 0.001 or less. Thus, the instrument limitations of the autotrackers on measuring optical depth typically appear to be within approximately 0.001 per instrument, barring filter center wavelength uncertainties in the short wavelength filters. However, atmospheric temporal turbidity variations often preclude Langley plot determination of optical depth with such a low error. Zero-airmass in-

tercept voltages, $V_{0\lambda}$, must then be relied on to recover τ_λ.

Example intercept voltages (in instrument A/D counts), for two wavelengths, obtained for some 51 days of observations in Tucson between October 1993 and June 1994 by autotracker 5 are plotted in Fig. 8. The days were selected/screened only to the extent that 1) they were clear, cloud-free days and 2) their Langley plots did not display significant departures from straight-line behavior (when such departures are visually apparent on a Langley plot, the intercept is most likely biased by at least a few percent). While there are evident day-to-day fluctuations in the intercepts, attributed to atmospheric variability, there is no indication of a substantial trend in the intercepts, leading to the conclusion that these channels maintained quite good stability over this 8-month observation period. Similar performance has been observed for other channels and instruments for such several month periods. However, intercept shifts and trends do eventually occur for some channels, due as best we can ascertain, to changes in interference filter transmittance, which can occur for a variety of reasons (dirt accumulation, film development, delamination of protective glass flats, crazing within filter, etc.).

Our approach to maintaining accurate intercept voltages and for monitoring instrument long-term stability has been to periodically make observations on several closely grouped very good observation days, usually on Mt. Lemmon, Arizona. The intercept results obtained from one such grouping of measurements made with autotracker 5 are shown in Fig. 9 for the 669-nm channel. Each data point is the Langley plot-derived intercept for a given day's observations (2–3 h of data collection after sunrise or before sunset). Also included on the

Langley Plot Intercepts for 669 nm Channel of Autotracker #5, May - June 1994
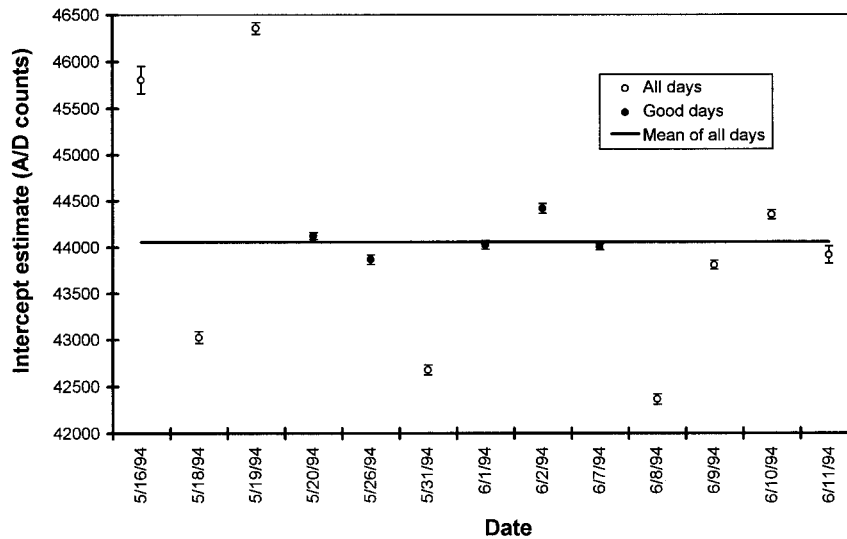

FIG. 9. Langley plot intercepts for 669-nm channel of autotracker 5, May–June 1994.

data points are the plus or minus one standard deviation error bars determined from the Langley plot fits. It is clearly evident that the Langley analysis typically underestimates the intercept uncertainty due, as best can be determined, to temporal variability in τ_λ. In a previous study (Reagan et al. 1987b) using data for some 50 days collected with one of the old manual solar radiometers, it was found that the Langley plot-derived intercept standard deviations underestimated the intercept departures from the apparent true intercept (determined from the mean of selected good day intercepts) by as much as a factor of 5 for two-thirds of all days.

The data for all observation days in the grouping used for Fig. 9 were screened to identify a subgroup of "good" days by applying several somewhat subjective tests (i.e., Langley plot obviously not straight; large scatter in Langley plot; slight curvature in Langley plot at large air mass; long wavelength optical depth too high, $\tau_\lambda > 0.003$ at 1030 nm; intercepts varying from mean of all intercept by $>2\sigma$; and optical depth standard deviations for several wavelengths too large, $\sigma_\tau > \sim 0.001$). It has been our experience that the means for all days and for only the good days are quite similar, but the standard deviation is generally much smaller for the good days subset, typically being less than 1% for wavelengths of 500 nm and greater.

Plots of mean intercepts for consecutive groups of days (i.e., each mean point determined from a group of days as in Fig. 9) for the 669- and 781-nm channels of autotracker 5 are given in Fig. 10 for a period spanning about 1 year. Means are included for both all days and the good days in each group, along with the plus or minus one standard deviation bars for the good days. It can be seen that the means for all days and only the good days

differ little from one another. The first six mean points are quite consistent for both channels. For example, the percent standard deviation for the first six good day points of the 669-nm channel is only about 0.3%, and the percent standard deviation of the mean of these six points is only about 0.12%. The last two points indicate a decreasing trend for the 669-nm channel, but no significant trend for the 781-nm channel. Subsequent measurements have confirmed a continuing downward trend in the 669-nm channel intercept with a decrease of approximately 9% over a 2-yr period. This apparent change in $V_{0\lambda}$ is not interpreted as something specific to the 669-nm wavelength region. Rather, it is most likely due to random interference filter degradation and might just as well have occurred at one of the other channel wavelengths (as has been observed with other instruments).

Maintaining an intercept record like that shown in Figs. 9 and 10 not only provides a running intercept calibration to use for instantaneous optical depth retrievals via Eq. (9) but also reveals instrument changes. If a channel intercept is in doubt, a corrected intercept can be determined for that channel based on a good intercept at another channel by using the transfer technique of Forgan (1994). New intercepts can also be estimated for a trending channel from limited sets of Langley plots, even if somewhat temporally corrupted, using various statistical and correlation analysis techniques (Harrison and Michalsky 1994; Erxleben and Reagan 1996), but investigation of these corrective approaches is beyond the intended scope of this paper. While there are numerous other data examples that could be presented, what has been given here suffices to demonstrate the capabilities of this new automated solar radiometer system.

Calibration Trends for Auto5, Selected Wavelengths
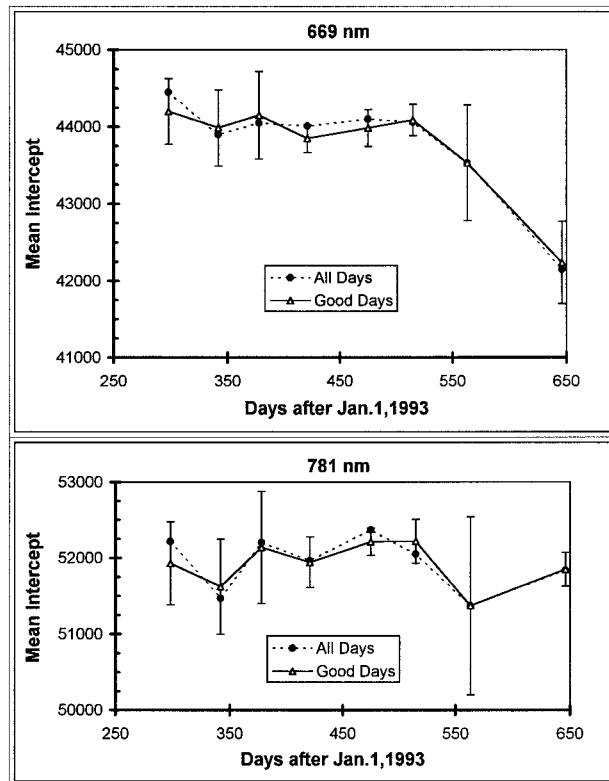### (Days are grouped together and averaged)

FIG. 10. Example calibration trends for autotracker 5 for 669- and 781-nm channels.

6. Concluding remarks

We have described the design features and presented example results demonstrating the performance of an automated multichannel solar radiometer. This instrument has been shown to perform reliably and with sufficient precision to permit accurate retrieval of optical depth, atmospheric conditions permitting. Several copies of the instrument are now in use for a variety of atmospheric sensing, atmospheric correction, and satellite ground-truthing applications.

Work continues in pursuit of further improvements and additions to the instrument. These include the following.

- Adding a passive tracking mode to the DAS to avoid instrument shutdown during extensive periods of intermittent cloudiness.
- Adding an offset voltage monitoring/correction option to the DAS to correct for the very small offset voltages that may be present at the output of the photodiode/op amp detector combination for each channel (offsets typically less than ± 100 counts, or less than 0.2% of the full count scale). Such offsets can contribute to slight errors in optical path retrievals [i.e., Eq. (10)] when the channel signal is much reduced from $V_{0\lambda}$,

as can occur for the short wavelength, high τ_{λ} channels at large air masses.

- Adding a diffuse light sensing channel at $\lambda \approx 780$ nm to monitor diffuse solar radiance in an annular ring around the sun (ring approximately 2° to 6° off sun center) to sense temporal variations in optical depth versus air mass. Having such a measurement would not only assist in identifying periods of temporally corrupted data but would also provide information that could be used to correct temporally biased Langley plot voltage intercept determinations (Forgan 1994). Results of implementing these instrumentation changes as well as more detailed analysis and interpretation of optical depth retrievals obtained with the existing instrument will be addressed in subsequent papers.

REFERENCES

Bruegge, C. J., R. Halthore, B. Markham, M. Spanner, and R. Wrigley, 1992: Aerosol optical depth retrievals over the Konza Prairie. *J. Geophys. Res.,* **97** (D17), 743–758.

Erxleben, W. H., and J. A. Reagan, 1996: An approach for obtaining best estimates of spectral optical depths and calibration intercepts from solar radiometer data corrupted by temporal variations. *IGARSS'96 Symp.,* Lincoln, NE, IEEE, 1014–1016.

Forgan, B. W., 1994: General method for calibrating sun photometers. *Appl. Opt.,* **33,** 4841–4850.

Harrison, L., and J. Michalsky, 1994: Objective algorithms for the retrieval of optical depths from ground-based measurements. *Appl. Opt.,* **33,** 5126–5132.

Herman, B. M., M. A. Box, J. A. Reagan, and C. M. Evans, 1981: Alternate approach to the analysis of solar photometer data. *Appl. Opt.,* **20,** 2925–2928.

Moore, A. S., L. E. Mauldin III, J. A. Reagan, C. W. Stump, and M. G. Fabert, 1989: Application of the Langley plot for calibration of sun sensors for the Halogen Occultation Experiment (HALOE). *Opt. Eng.,* **28,** 180–187.

Reagan, J. A., L. W. Thomason, B. M. Herman, and J. M. Palmer, 1986: Assessment of atmospheric limitations on the determination of the solar spectral constant from ground-based spectroradiometer measurements. *IEEE Trans. Geosci. Remote Sens.,* **GE-24,** 258–266.

——, P. A. Pilewskie, I. C. Scott-Fleming, B. M. Herman, and A. Ben-David, 1987a: Extrapolation of Earth-based solar irradiance measurements to exoatmospheric levels for broadband and selected adsorption-band observations. *IEEE Trans. Geosci. Remote Sens.,* **GE-25,** 647–653.

——, I. C. Scott-Fleming, and B. M. Herman, 1987b: Effects of temporal variations in optical depth on the determination of the optical depth and solar constant from solar photometry. *Atmospheric Radiation: Progress and Prospects,* K.-N. Liou and Z. Xiuji, Eds., Science Press and Amer. Meteor. Soc., 571–577.

Slater, P. N., S. F. Biggar, R. G. Holm, R. D. Jackson, Y. Mao, M. S. Moran, J. M. Palmer, and B. Yuan, 1987: Reflectance and radiance-based methods for the in-flight absolute calibration of multispectral sensors. *Remote Sens. Environ.,* **22,** 11–37.

Teillet, P. M., P. N. Slater, Y. Ding, and R. P. Santer, 1990: Three methods for the absolute calibration of the NOAA AVHRR sensors in-flight. *Remote Sens. Environ.,* **31,** 105–120.